

Notice: This manuscript has been authored by UT-Battelle, LLC under Contract No. DE-AC05-00OR22725 with the U.S. Department of Energy. The United States Government retains and the publisher, by accepting the article for publication, acknowledges that the United States Government retains a non-exclusive, paid-up, irrevocable, world-wide license to publish or reproduce the published form of this manuscript, or allow others to do so, for United States Government purposes. The Department of Energy will provide public access to these results of federally sponsored research in accordance with the DOE Public Access Plan (<http://energy.gov/downloads/doe-public-access-plan>).

Effect of Impurities on the Compatibility of Steels in Supercritical CO₂ at 450°-650°C

Bruce A. Pint, Michael J. Lance, Rishi Pillai and James R. Keiser

Materials Science & Technology Division, Oak Ridge National Laboratory, P.O. Box 2008, Oak Ridge, TN 37831-6156 USA (pintba@ornl.gov, 865-576-2897)

ABSTRACT

Direct-fired supercritical CO₂ (sCO₂) power cycles are a pathway to low-CO₂ fossil energy but contain O₂ and H₂O in the sCO₂ from combustion. The effect of impurities on structural steels was investigated at 450°-650°C in 30 MPa sCO₂. The test matrix included 9 and 12%Cr ferritic-martensitic (FM) steels and conventional and advanced austenitic steels exposed for 1000-2000 h with and without additions of 1%O₂ and 0.1%H₂O to simulate the cycle after water removal. For FM steels, the mass gains and scale thicknesses were similar with and without impurities with the formation of thick, duplex Fe-rich scales in all cases including the observation that Fe₂O₃ only formed with 1%O₂. For the austenitic steels, higher mass gains were observed at all temperatures with increased formation of Fe-rich oxides when impurities were added. Carbon ingress was assessed by bulk combustion analysis, glow discharge optical emission spectroscopy and measuring post-exposure room temperature tensile properties. Bulk C content was strongly increased at 650°C but not at 450° or 550°C.

Keywords: Oxidation, High Temperature Materials, High Pressure Testing, Experimental Work

1. INTRODUCTION

A number of power generation technologies are exploring the use of supercritical CO₂ (sCO₂) including nuclear, fossil, concentrating solar power (CSP), geothermal and waste heat recovery, because of its unique properties and relatively low critical point (31°C/73.8 bar) [1-7]. Laboratory studies over the past decade have suggested that Ni-based alloys have reasonable compatibility with sCO₂ at temperatures of $\geq 700^\circ\text{C}$ [8-17], where greater than 50% thermal efficiency is predicted [1]. However, for sCO₂-based cycles to be commercially competitive, lower cost steels are needed for the lower temperature components. Based on historical experience, there is a significant

concern about the use of steels in sCO₂ because of prior experience with Grade 9 (Fe-9Cr-1Mo) steel in the UK advanced gas cooled reactors (AGRs) operated with sub-critical 43 bar CO₂ at <550°C where severe internal carburization could occur [18]. A recent review concluded that 9-12%Cr ferritic-martensitic (FM), or sometimes called creep-strength enhanced ferritic (CSEF) steels, were limited to 450°C in sCO₂ [19], significantly lower than the 580°-600°C limit in supercritical steam [20]. A nuclear fuel cladding study found that an austenitic stainless steel such as type 316FR had much better oxidation resistance in sCO₂ than CSEF steels but began to show accelerated oxidation at 600°C [21]. However, advanced, highly alloyed austenitic steels have been observed to have low C ingress at 750°C [16]. The driving force for C ingress is that the carbon activity (a_c) at the metal-oxide interface can be much higher than the activity in the gas due to the low interfacial oxygen partial pressure with very stable oxide scales [22]. A dense and adherent Cr-rich oxide scale may be an effective barrier to C ingress [23].

Another factor in assessing sCO₂ steel compatibility is the presence of impurities in the sCO₂. At 750°C, little difference in reaction rates was noted between research grade (RG) sCO₂ with < 5ppm H₂O and < 5 ppm O₂ and industrial grade (IG) sCO₂ with < 50 ppm O₂ and 18±16 ppm H₂O, Figure 1 [15,16,24]. However, the higher impurity levels expected for the direct-fired Allam cycle [5,7] compared to indirect-fired or closed cycles, has been shown to affect reaction rates [11,15,17]. Also, the additions (CH₄, H₂O, etc.) in the AGR CO₂ [18] used to lower the O₂ partial pressure to prevent oxidation of the graphite moderator may have affected performance.

This ongoing laboratory study [25-27] has exposed two CSEF steels and two austenitic steels to 30 MPa RG sCO₂ at 450°-650°C for up to 2000 h (using 500-h cycles) to better assess the maximum use temperatures for these materials in sCO₂ with and without impurities. Controlled O₂ and H₂O additions were used to simulate the Allam cycle after water removal at 30 MPa. A similar study with 1%O₂ and 4%H₂O contents simulated the sCO₂ after combustion [17]. In addition to measuring mass change and characterizing the oxide thickness and composition, room temperature tensile properties and bulk C content [28,29] have been measured to assess internal carburization. Glow discharge optical emission spectroscopy (GDOES) was used to characterize C ingress.

2. MATERIALS AND METHODS

Table 1 lists the measured chemical compositions of the materials reported in this study. Specimen coupons (~12 x 20 x 1.5mm) and dogbone tensile specimens (SS-3 type: 25.4 mm long, 0.76 x 5 mm gauge) were prepared with a 600 grit finish and ultrasonically cleaned in acetone and methanol prior to exposure. Specimens were exposed in RG sCO₂ (<5 ppm O₂, <5 ppm H₂O) for 500-h cycles in a vertically-oriented autoclave (~266 mm x 83

mm inner diameter) machined from alloy 282 with an alloy 282 specimen rack. The autoclave was heated inside a three-zone furnace and the fluid flow rate was ~ 2 ml/min. The specimens were heated to temperature over several hours ($\sim 2^\circ\text{C}/\text{min}$) in 30 MPa sCO_2 , held at temperature $\pm 2^\circ\text{C}$ and then cooled in sCO_2 to room temperature. For the controlled impurity experiments, two pumps, for sCO_2 and H_2O , were used, and O_2 was added as a $\text{CO}_2\text{-O}_2$ gaseous mixture from a high pressure cylinder. Based on gas flow rates, the O_2 was calculated as $1.0 \pm 0.2\%$ and the H_2O content as $0.1 \pm 0.05\%$ with the largest variations associated with issues with filters, valves and changing sCO_2 cylinders (usually twice per 500-h cycle). Additional details about the experiment have been previously provided [10,12,15,16,25-27].

The specimens were weighed before and after exposure using a Mettler Toledo model XP205 balance with an accuracy of ± 0.04 mg. Room temperature tensile tests used a strain rate of 0.015/min per ASTM E8-13. Bulk C was measured using combustion analysis and C profiles were measured using GDOES to quantify the C uptake using the starting measured composition in Table 1 as a reference [30]. For metallography, specimens with thin reaction products were copper plated before being sectioned. Polished sections were then characterized using light microscopy and secondary electron microscopy (SEM) equipped with energy dispersive x-ray spectroscopy (EDS), using a TESCAN model MIRA3. Reaction product thickness was measured using image analysis software with at least 30 measurements taken per specimen.

3. RESULTS AND DISCUSSION

As mentioned above, Figure 1 provides background information on the effect of impurities at 750°C where steels would not likely be used. The low impurity levels (e.g. 18 ± 16 ppm H_2O measured in 10 gas cylinders [16]) in IG sCO_2 did not significantly change the median mass change after 1000 h at 750°C compared to RG sCO_2 . However, the addition of $1\%\text{O}_2$ and $0.25\%\text{H}_2\text{O}$ in this earlier study caused significant changes, especially for the Fe-based alloys. The largest mass changes were observed for the lowest alloyed steel, type 304H, Table 1. When the $1\%\text{O}_2$ and $0.25\%\text{H}_2\text{O}$ were added individually, all of the steels, 304H, 25SS (Sanicro 25) and 310HN (310HCbN or HR3C)) were more strongly attacked by the $\text{sCO}_2+1\%\text{O}_2$ environment, with similar mass changes as the $\text{sCO}_2+1\%\text{O}_2+0.25\%\text{H}_2\text{O}$ environment, Figure 1. The Ni-based alloys were not as strongly affected by the impurity additions except for the low Cr superalloy 247 (MarM247).

Now focusing on the four steels (T91, VM12, 316H and 709), the sCO₂ exposures were conducted at 450°-650°C and the mass change data has been reported previously [25-27]. Figure 2 shows the rate constants generated from the 2-4 median mass gain data points (after 2-4 500-h cycles) from 5-6 specimens of each alloy at each condition. The rate constants were generated using a standard method [31] and are compared to values from the literature in sCO₂ without impurities [9,21] shown as small circles. For both 316H and FM steels, the results in RG sCO₂ are very similar to the literature values. A metric developed for CSP applications is shown as a horizontal dashed line in Figure 2. Below this rate, which would only be achieved with a slower-growing Cr-rich oxide scale, scale spallation is not expected to be significant for a 100,000 h component lifetime [16]. Example rates for Ni-based 740H are well below the metric at 800°C in RG sCO₂. While basing a rate on only 2 data points is not ideal, prior work indicated that the rate calculated after 1,000 h (2 cycles) was very similar to that calculated after 10,000 h exposures [16]. Selected longer exposures of these steels to at least 2,000 h (4, 500-h cycles) are currently in progress.

For the FM/CSEF steels, the rates were very high under these conditions and little benefit was observed for the higher Cr content in VM12 compared to T91, Table 1. As has been reported in several studies [21,32,33], FM steels form duplex Fe-rich oxides in sCO₂ and representative examples at each temperature are shown in Figure 3. It should be noted that the rates observed for these FM steels are almost identical to those measured after 1000 h exposures in 28 MPa H₂O [34] shown in Figure 2. Also, it has been reported previously that Cr enrichment does not occur in the Fe-rich scale formed in steam at 550°C and below [35] because the Cr diffusion rate is too slow [36]. Thus, higher Cr contents may be more effective at higher temperatures or might show a benefit for longer exposure times.

Consistent with the rate data in Figure 2, the addition of O₂/H₂O impurities increased the reaction rate on the T91 specimens at 450°C, resulting in a thicker oxide, Figures 3a and 3b. Figure 4 shows that the oxide thickness on both FM steels after 1000 h exposures was affected by impurities with the oxide becoming more porous and less dense with examples shown in Figure 3. At higher temperatures, the addition of impurities did not significantly increase the scale thickness or change the rate constants, Figure 2. However, the higher O₂ partial pressure with 1%O₂ did result in the formation of a Fe₂O₃ outer layer on all of the FM steel specimens, with examples in Figures 3d and 3f, where Fe₂O₃ appears lighter using light microscopy. In RG sCO₂, only Fe₃O₄ was observed in the outer layer. In both environments, an inner (Fe,Cr)₃O₄ layer formed.

For the stainless steels, thin oxides formed at 450°C in both environments [27] with minor increases in the thickness measured with impurities, Figure 4. In RG sCO₂, the mass gains were very low for the alloy 709 samples resulting in very low rates in this temperature range, Figure 2, similar to rates measured for Ni-based alloys [9,16]. Figure 5 shows images of the scales formed on 316H and 709 specimens after exposures at 550° and 650°C. As reported earlier [25-27], even in RG sCO₂, 316H was not able to form a protective Cr-rich scale at 650°C, Figure 5g. For the other cases, the increase in scale thickness with the addition of impurities was very dramatic, Figures 4 and 5.

Characterization of the reaction products formed in RG sCO₂ at 650°C using SEM/EDS was reported previously [25]. Figures 6 and 7 show SEM/EDS analysis of the scales formed at 650°C in sCO₂+1%O₂+0.1%H₂O. A rate constant was not reported for 316H at 650°C in sCO₂+1%O₂+0.1%H₂O because the specimens lost mass due to spallation of the outer, Fe-rich oxide layer. However, comparing Figures 5g and 5h, an outer Fe₂O₃ layer was retained on the surface after exposure in sCO₂+1%O₂+0.1%H₂O. An Fe₂O₃ layer would not be expected to form in RG sCO₂ without impurities and the outer Fe₂O₃ layer in Figure 5h may have regrown during the second 500 h cycle. No outer layer was observed after sectioning the 316H specimen exposed in RG sCO₂, Figure 5g. The inner scale looked similar in both environments with Ni-enriched in this layer (Figure 6f) that is typically a mixture of metal and oxide [37]. The enrichment of Cr observed in Figure 6b may be due to initial carbide formation along alloy grain boundaries that was subsequently consumed by the oxidation front.

For alloy 709, the addition of impurities resulted in an apparent duplex oxide structure at both 550° and 650°C, Figures 5b and 5f. Figure 7 shows that the inner layer formed at 650°C is Cr-rich while the outer layer is Fe-rich. In this case, Ni appears to be enriched in the underlying alloy with only a few Ni-rich precipitates incorporated into the much thinner reaction product. A line profile (not shown) measured a Ni content of ~40 wt.% near the alloy surface where the Cr content was depleted to ~8.5%.

The focus on mass change and oxide thickness does not address the issue of C ingress and the possibility of degrading the mechanical properties, thereby reducing the maximum use temperature of steels in sCO₂. The tensile properties after 500 and 1000 h exposures have been previously reported [25-27]. Of particular interest is embrittlement and 316H showed a strong effect of temperature. Figure 8 summarizes the effect on total elongation (i.e. ductility) as a function of specimen mass change. The small mass changes measured at lower temperature reflect the formation of a Cr-rich oxide. The addition of impurities (closed symbols) increased the mass gain but did

not affect ductility at 450° and 550°C after 500-1000 h. However, at 650°C where the highest mass gains were measured due to the formation of a thick Fe-rich reaction product, Figures 5g and 5h, the total elongation was significantly reduced suggesting embrittlement due to C ingress. Using bulk C measurements from the entire 316H coupon specimen, only after exposure at 650°C for 1000 h was the C content strongly increased, Figure 9. Similar C ingress results are reported for T91 and VM12. In contrast, alloy 709 only showed a minor increase in C content after 1000 h at 650°C with impurities where a duplex scale was observed, Figures 5f and 7. Room temperature tensile testing of alloy 709 only showed a 50% drop in ductility after exposures at 650°C in sCO₂ with impurities [39]. There was some general indication that the addition of impurities in the sCO₂ increased C ingress at 650°C but not for all materials. More measurements are needed to improve the statistics and additional measurements will be made after 2,000 h exposures at 550° and 650°C. Especially at 550°C, longer exposures may reveal increased C contents using this method.

The bulk C content measurements in Figure 9 do not provide any information about the C distribution or profile in the steels. To gain more information, C profiles were measured using GDOES, Figure 10. Note that these results are in at.% whereas C values in Figure 9 were wt.%. For 316H specimens exposed for 1000 h, there appeared to be very little C ingress at 450°C with or without impurities. After exposure at 650°C, Figure 10a shows large C peaks observed in the substrate after sputtering through the thick inner oxide layer shown in Figures 5g and 5h. At 650°C, the C peak was higher when impurities were present in the sCO₂. However, more C ingress was detected without impurities at 550°C, Figure 10a. For alloy 709, only 650°C specimens were examined and both Cr and C profiles are shown in Figure 10b. No C ingress was detected after exposure to RG sCO₂ while a significant peak was observed when impurities were added and the scale was duplex and contained Fe, Figures 5f and 7. This result supports the hypothesis [16,23,40] that thin Cr-rich oxides (i.e. Figure 5e) are good barriers to C ingress and the formation of a duplex scale when impurities are added degrades the protection. A remaining concern is if a higher alloyed steel like 709 can continue to form a protective Cr-rich scale after much longer exposures in sCO₂. High-resolution analytical transmission electron microscopy has found Cr-C-O phases forming within the Cr-rich scale formed on alloy 709 in RG sCO₂ at 650°C [41,42]. Previously, 25SS (Table 1) tested for 10,000 h at 750°C in IG sCO₂ showed no evidence of C ingress [16]. However, longer testing at lower temperatures may be needed.

The next stage of the project is modeling C ingress and exploring the potential benefit of coatings [43,44] or surface modifications to increase the temperature window for using less expensive steels in sCO₂ applications. The

goal is to use the current short term information to predict C ingress after 100,000 h, especially at 550°-650°C where stainless steels might replace Ni-based alloys and at 450°-550°C where CSEF steels might replace more expensive (and lower strength) austenitic steels. In addition to degrading the mechanical properties, significant long-term C ingress might also accelerate scale growth rates.

CONCLUSION

The sCO₂ compatibility of four representative steels was investigated in sCO₂ with and without 1%O₂ and 0.25%H₂O impurities at 30 MPa using 500-h cycles at 450°-650°C. This level of impurities did not significantly change the reaction rates for 9-12%Cr FM steels above 450°C but increased reaction rates for both stainless steels at 450°-650°C with the formation of a duplex Fe-rich scale at 550° and 650°C. The formation of Fe-rich scales was correlated with C ingress and a drop in post exposure ductility, especially for 316H at 650°C. There was not a clear correlation between the addition of impurities and increased C ingress.

ACKNOWLEDGMENTS

The authors would like to thank EPRI for supplying the VM12 material, Tenaris for supplying T91 and S. Sham at INL for the 709 material from the ASME code case project. At ORNL, B. Johnston, M. Howell, T. M. Lowe, K. L. Hedrick and V. Cox for assistance with the experimental work. Y.-F. Su and M. Ridley provided helpful comments on the manuscript. This research was sponsored by the U.S. Department of Energy, Office of Fossil Energy and Carbon Management, Advanced Materials Program.

REFERENCES

- [1] Feher, E. G., 1968, "The Supercritical Thermodynamic Power Cycle," *Energy Conversion*, **8**, pp.85-90.
- [2] Dostal, V., Hejzlar, P. and Driscoll, M. J., 2006, "High-Performance Supercritical Carbon Dioxide Cycle for Next-Generation Nuclear Reactors," *Nuclear Technology*, **154**(3), pp.265-282.
- [3] Chen, H., Goswami, D. Y. and Stefanakos, E. K., 2010, "A review of thermodynamic cycles and working fluids for the conversion of low-grade heat," *Renewable & Sustainable Energy Reviews* **14**, pp.3059-3067.
- [4] Iverson, B. D., Conboy, T. M., Pasch, J. J. and Kruijenga, A. M., 2013, "Supercritical CO₂ Brayton cycles for solar-thermal energy," *Applied Energy*, **111**, pp.957-970.
- [5] Allam, R. J., Palmer, M. R., Brown, G. W., Fetvedt, J., Freed, D., Nomoto, H., Itoh, M., Okita, N., Jones, C., 2013, "High efficiency and low cost of electricity generation from fossil fuels while eliminating atmospheric emissions, including carbon dioxide," *Energy Procedia*, **37**, pp.1135-1149.

[6] Oh, C. H., Lillo, T., Windes, W., Totemeier, T., Ward, B., Moore, R., Barner, R., 2006, "Development Of A Supercritical Carbon Dioxide Brayton Cycle: Improving VHTR Efficiency And Testing Material Compatibility," Idaho National Laboratory Report INL/EXT-06-01271.

[7] Allam, R., Martin, S., Forrest, B., Fetvedt, J., Lu, X., Freed, D., Brown Jr., G. W., Sasaki, T., Itoh, M., Manning, J. , 2017, "Demonstration of the Allam Cycle: An Update on the Development Status of a High Efficiency Supercritical Carbon Dioxide Power Process Employing Full Carbon Capture," Energy Procedia, **114**, pp.5948-5966.

[8] Olivares, R. I., Young, D. J., Marvig, P. and Stein, W., 2015, "Alloys SS316 and Hastelloy-C276 in Supercritical CO₂ at High Temperature," Oxidation of Metals **84**, pp.585–606

[9] Dheeradhada, V., Thatte, A., Karadge, M. and Drobnjak, M., 2015, "Corrosion of Supercritical CO₂ Turbomachinery Components," in Proceedings of the EPRI International Conference on Corrosion in Power Plants, Oct. 2015, San Diego, CA.

[10] Pint, B. A. and Keiser, J. R., 2015, "Initial Assessment of Ni-Base Alloy Performance in 0.1 MPa and Supercritical CO₂," JOM **67**, pp.2615-2620.

[11] Mahaffey, J., Adam, D., Brittan, A., Anderson M., Sridharan, K., 2016, "Corrosion of Alloy Haynes 230 in High Temperature Supercritical Carbon Dioxide with Oxygen Impurity Additions," Oxidation of Metals, **86**, 567-580.

[12] Pint, B. A., Brese, R. G. and Keiser, J. R., 2017, "Effect of Pressure on Supercritical CO₂ Compatibility of Structural Alloys at 750°C," Materials and Corrosion, **68**, pp.151-158.

[13] Oleksak, R. P., Tylczak, J. H., Carney, C. S., Holcomb, G. R., Doğan, O. N., 2018, "High-Temperature Oxidation of Commercial Alloys in Supercritical CO₂ and Related Power Cycle Environments," JOM, **70**, pp.1527-1534.

[14] Olivares, R. I., Young, D. J., Nguyen, T. D., Marvig, P., 2018, "Resistance of High-Nickel, Heat-Resisting Alloys to Air and to Supercritical CO₂ at High Temperatures," Oxidation of Metals, **90**, 1-25.

[15] Pint, B. A., Lehmusto, J., Lance, M. J., Keiser, J. R., 2019, "The Effect of Pressure and Impurities on Oxidation in Supercritical CO₂," Materials and Corrosion, **70**, pp.1400-1409.

[16] Pint, B. A., Pillai, R., Lance M. J., Keiser, J. R., 2020, "Effect of Pressure and Thermal Cycling on Long-Term Oxidation in CO₂ and Supercritical CO₂" Oxidation of Metals, **94**, pp.505–526.

[17] Oleksak, R. P., Carney, C. S., Doğan, O. N., 2023, “Effect of pressure on high-temperature oxidation of Ni alloys in supercritical CO₂ containing impurities,” *Corrosion Science* **215**, 111055.

[18] Gong, Y., Young, D. J., Kontis, P., Chiu, Y. L., Larsson, H., Shin, A., Pearson, J. M., Moody M. P., Reed, R. C., 2017, “On the breakaway oxidation of Fe₉Cr₁Mo steel in high pressure CO₂,” *Acta Materialia*, **130**, pp.361-374.

[19] Sarrade, S., Férona, D., Rouillard, F., Perrin, S., Robin, R., Ruiz, J. C., Turc, H. A., 2017, “Overview on corrosion in supercritical fluids,” *Journal of Supercritical Fluids*, **120**, pp.335–344.

[20] Shingledecker, J. P., Pint, B. A., Sabau, A. S., Fry, A. T., Wright, I. G., 2013, “Managing Steam-Side Oxidation and Exfoliation in USC Boiler Tubes,” *Advanced Materials and Processing*, **171**(1), pp.23-25.

[21] Furukawa, T., Inagaki, Y., Aritomi, M., 2011, “Compatibility of FBR structural materials with supercritical carbon dioxide,” *Progress in Nuclear Energy* **53**, 1050–1055.

[22] Gheno, T., Monceau, D., Zhang, J., Young, D. J., 2011, “Carburisation of Ferritic Fe-Cr Alloys by Low Carbon Activity Gases,” *Corrosion Science*, **53**, pp.2767-2777.

[23] Meier, G. H. Coons, W. C., Perkins, R. A., 1982, “Corrosion of Iron-, Nickel- and Cobalt-Base Alloys in Atmospheres Containing Carbon and Oxygen,” *Oxidation of Metals*, **17**, pp.235-262.

[24] Lehmusto, J., Ievlev, A. V., Keiser, J. R., Pint, B. A., 2021, “A tracer study on sCO₂ corrosion with multiple oxygen-bearing impurities,” *Oxidation of Metals* **96**, pp.571-587.

[25] Pint, B. A., Pillai, R., Keiser, J. R., 2021, “Effect of Supercritical CO₂ on Steel Ductility at 450°-650°C” ASME Paper #GT2021-59383, for Turbo Expo 2021 Virtual Conference and Exhibition, June 11-15, 2021.

[26] Pint, B. A., Pillai, R., Keiser, J. R., 2021, “Compatibility of Steels in Supercritical CO₂ at 450°-650°C,” AMPP Paper C2021-16724, Houston, TX, presented virtually at Corrosion 2021.

[27] Pint, B. A., Lance M. J., Pillai, R., Keiser, J. R., 2022, “Compatibility of Steels at 450°-650°C in Supercritical CO₂ with O₂ and H₂O Additions” AMPP Paper C2022-18018, Houston, TX, virtual presentation at Corrosion 2022.

[28] McCoy, H. E., 1965, “Type 304 Stainless Steel vs. Flowing CO₂ at Atmospheric Pressure and 1100-1800°F,” *Corrosion*, **21**, pp.84-94.

[29] Martin, W. R. and Weir, J. R., 1965, “Influence of Chromium Content on Carburization of Chromium-Nickel-Iron Alloys in Carbon Dioxide,” *Journal of Nuclear Materials*, **16**, pp.19-24.

[30] Lance, M. J., Leonard, D. N., Pint, B. A., 2018, "The Use of Glow Discharge Optical Emission Spectroscopy to Quantify Internal Carburization in Supercritical CO₂," in Proceedings of the 6th International Symposium on Supercritical CO₂ Power Cycles, Pittsburgh, PA, Paper #117.

[31] Pieraggi, B., 1987, "Calculations of Parabolic Reaction Rate Constants," *Oxidation of Metals* **27**, pp.177-85.

[32] Rouillard, F., Charton, F. and Moine, G., 2011, "Corrosion Behavior of Different Metallic Materials in Supercritical Carbon Dioxide at 550°C and 250 bars," *Corrosion* **67** (9), 095001.

[33] Tan, L., Anderson, M., Taylor, D., Allen, T. R., 2011, "Corrosion of austenitic and ferritic-martensitic steels exposed to supercritical carbon dioxide," *Corrosion Science*, **53**, 3273-3280.

[34] Pint, B. A., Pearson, S. R., De Las Casas Aranda, R., Lance, M. J., Raiman, S. S., Kung, S. C., 2019 "Water Chemistry and Pressure Effects on Steam Oxidation of Ferritic and Austenitic Steels," in Proceedings of the Joint EPRI – 123HiMAT International Conference on Advances in High Temperature Materials, J. Shingledecker and M. Takeyama eds., ASM International, Materials Park, OH, pp.939-947.

[35] Kurley, J. M., Pint, B. A., 2020, "The Effect Of Shot Peening On Steam Oxidation Of 304H Stainless Steel," *Oxidation of Metals*, **93**, pp.159-174.

[36] Tökei, Zs., Hennesen, K., Viehhaus, H. and Grabke, H. J., 2000, "Diffusion of Chromium in Ferritic and Austenitic 9-20 Wt.% Chromium Steels," *Materials Science Technology*, **16**, pp.1129-1138.

[37] Peraldi, R. and Pint, B. A., 2004, "Effect of Cr and Ni Contents on the Oxidation Behavior of Ferritic and Austenitic Model Alloys in Air With Water Vapor," *Oxid. Met.*, **61**, pp.463-83.

[38] Pint, B. A., 2021, "High temperature compatibility of structural alloys with supercritical and subcritical CO₂," *Interface*, **30**, pp.67-71.

[39] Pint, B. A., Pillai, R., Lance, M. J., Keiser, J. R., 2024, "Coated and Uncoated Steel Compatibility in Supercritical CO₂ at 450°-650°C," in Proceedings of the 8th International Symposium on Supercritical CO₂ Power Cycles, San Antonio, TX, February 2024, Paper #113.

[40] Oleksak, R. P., Holcomb, G. R., Carney, C. S., Doğan, O. N., 2022, "Carburization susceptibility of chromia-forming alloys in high-temperature CO₂," *Corros. Sci.* **206**, 110488.

[41] Pint, B. A., Su, Y.-F., Lance, M. J., Pillai, R., Keiser, J. R., 2023, "Internal Carburization and Scale Formation on Austenitic Steels in Supercritical Carbon Dioxide," *Materials at High Temperature*, **40**, pp.308-317.

[42] Pint, B. A., Su, Y.-F., Pillai, R., 2024, “Characterization of Oxide Scales Formed on Fe-20Cr-(20-25)Ni Alloys in Supercritical CO₂,” AMPP Paper C2024-21218, Houston, TX, to be presented at AMPP Annual Meeting, March 2024, New Orleans, LA.

[43] Pint, B. A., Pillai, R., Keiser, J. R., 2022, “Evaluation of Coatings to Improve Steel Compatibility in Supercritical CO₂,” AMPP Paper C2023-19207, Houston, TX.

[44] Pint, B. A., Su, Y.-F., Lance, M. J., Pillai, R., Keiser, J. R., 2022, “Evaluation of Coated Steels in Supercritical CO₂,” Materials and Corrosion, *in press*, 2024.

Table 1. Alloy chemical composition (mass %, balance Fe) determined by plasma and combustion analyses.

Alloy	Cr	Ni	Mo	Mn	Si	C	S*	Other
T91	8.6	0.3	0.9	0.5	0.4	0.10	6	0.2V,0.06Nb,0.045N
VM12	11.5	0.4	0.4	0.4	0.4	0.12	3	1.6W,1.5Co,0.2V,0.04N
316H	16.3	10.0	2.0	0.8	0.5	0.04	6	0.3Cu,0.3Co,0.04N
709	20.1	25.2	1.5	0.9	0.4	0.06	3	0.2Nb,0.06Cu,0.15N
304H	18.3	8.6	0.3	1.8	0.3	0.07	51	0.4Cu,0.2Co,0.06N
310HN	25.5	20.3	0.1	1.2	0.3	0.05	4	0.3Co,0.4Nb,0.3N
25SS	22.3	25.4	0.2	0.5	0.2	0.07	8	3.4W,3Cu,1.5Co,0.5Nb
625	21.7	61.0	8.8	0.2	0.2	0.02	<3	4Fe,3.5Nb,0.2Ti,0.1Al
230	22.6	60.5	1.4	0.5	0.4	0.10	9	12.3W,1.5Fe,0.3Al
740H	24.5	49.7	0.3	0.3	0.2	0.03	17	21Co,1.5Nb,1.4Ti,1.4Al
282	19.6	57.1	8.6	0.02	0.04	0.06	<3	10.6Co,2.2Ti,1.6Al
247	8.5	59.5	0.7	<	0.03	0.16	<3	10Co,10W,3Ta,6Al,1.4Hf

* S in ppmw < signifies less than 0.002

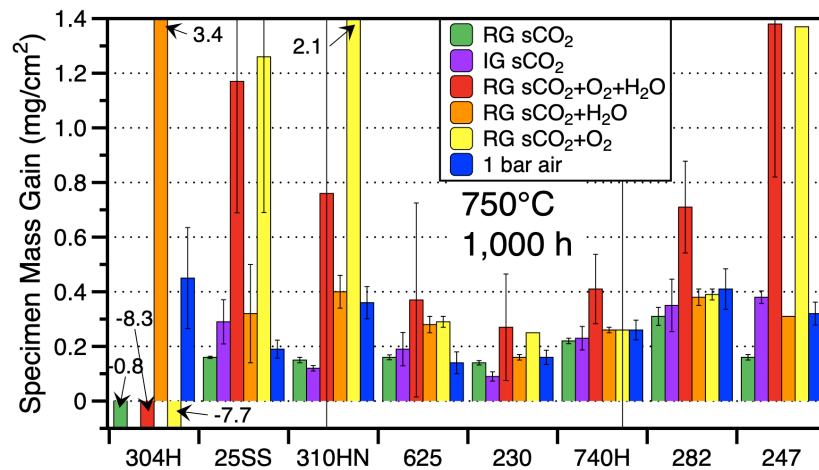


Figure 1: Median mass gain of specimens in various environments after 1000 h at 750 °C. Some data previously reported [15,16].

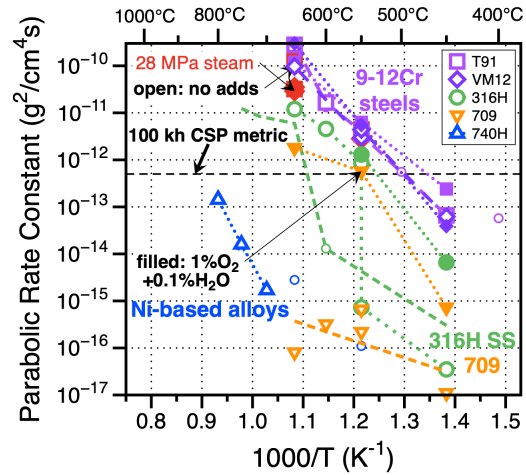


Figure 2: Arrhenius plot of literature values (small circles [9,20]) and rate constants from this study in 30 MPa RG sCO₂ (open symbols) and RG sCO₂ with 1%O₂ + 0.1%H₂O (solid symbols). Some data previously reported [16,25-27,34].

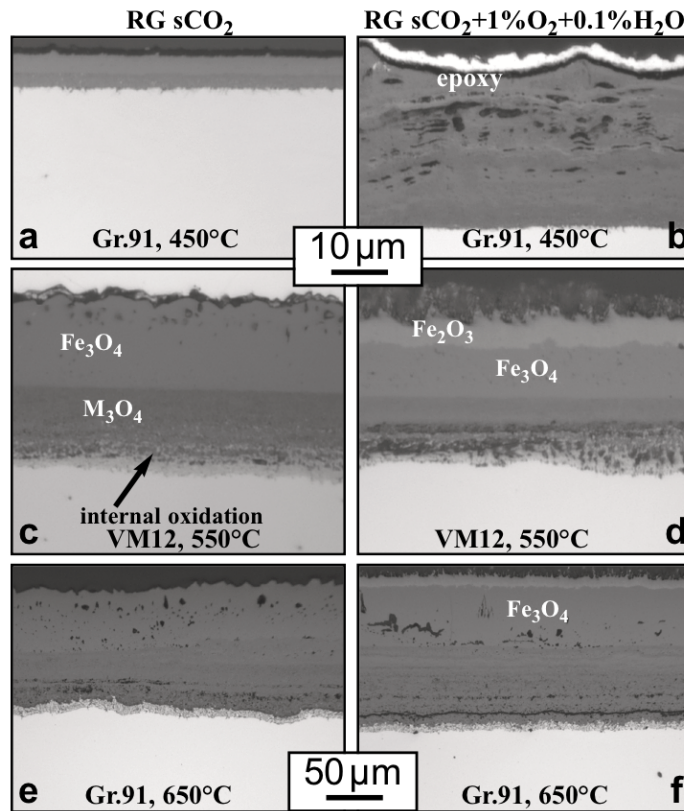


Figure 3: Light microscopy of polished cross-sections of (a,b,e,f) Grade 91 and (c,d) VM12 exposed for 1000 h at (a,b) 450°C, (c,d) 550°C and (e,f) 650°C in (a,c,e) RG sCO₂ and (b,d,f) RG sCO₂+1%O₂+0.1%H₂O.

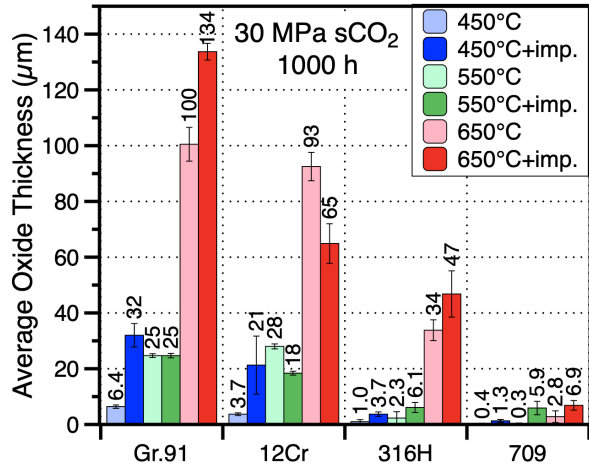


Figure 4: Average oxide thickness after 1,000 h exposure in 30 MPa RG sCO₂ at each condition. The whiskers show one standard deviation. Data adapted from [27].

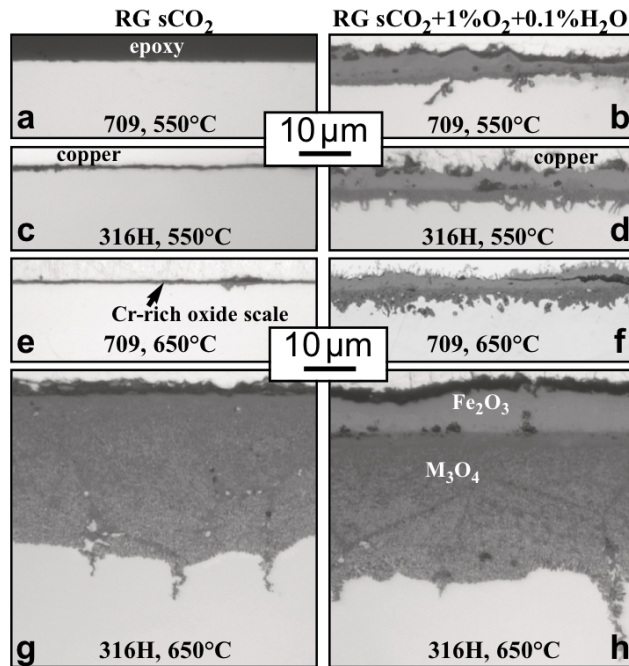


Figure 5: Light microscopy of polished cross-sections of (a,b,e,f) 709 and (c,d,g,h) 316H exposed for 1000 h at (a-d) 550°C and (e-h) 650°C in (a,c,e,g) RG sCO₂ and (b,d,f,h) RG sCO₂+1%O₂+0.1%H₂O.

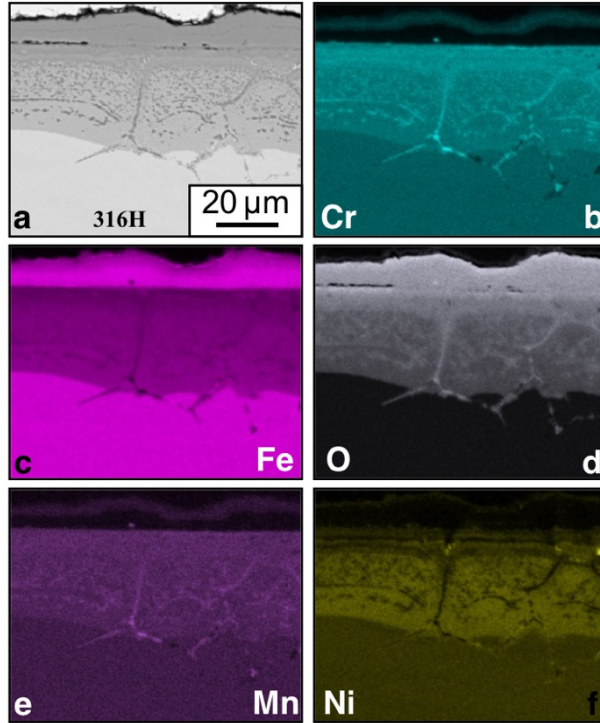


Figure 6: (a) SEM secondary electron image of the inner scale formed on 316H after 1000 h at 650°C in $s\text{CO}_2+1\%\text{O}_2+0.1\%\text{H}_2\text{O}$ and (b-f) EDX maps of the same region.

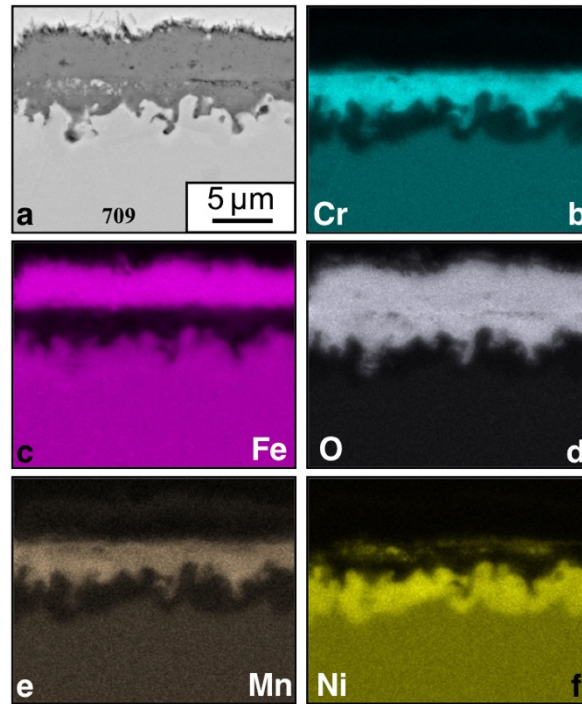


Figure 7: (a) SEM secondary electron image of the scale formed on 709 after 1000 h at 650°C in $s\text{CO}_2+1\%\text{O}_2+0.1\%\text{H}_2\text{O}$ and (b-f) EDX maps of the same region.

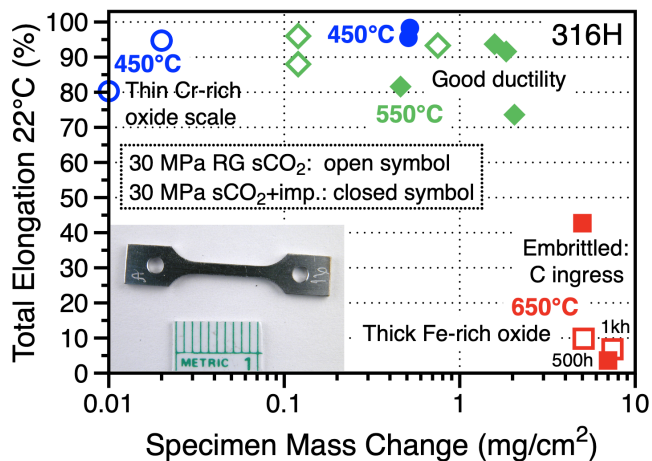


Figure 8: Mass change of 316H specimens plotted versus post-exposure room temperature total elongation for 500 and 1000 h exposures in 30 MPa RG sCO₂ (open symbols) and RG sCO₂ with 1%O₂ + 0.1%H₂O (solid symbols). The RG sCO₂ data was previously reported [38].

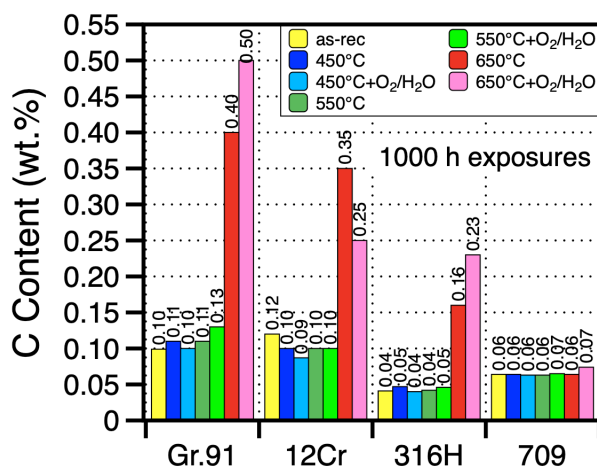


Figure 9: Alloy C content measured after 1000 h exposures in each environment using combustion analysis and compared to starting C content. Some data adapted from [27].

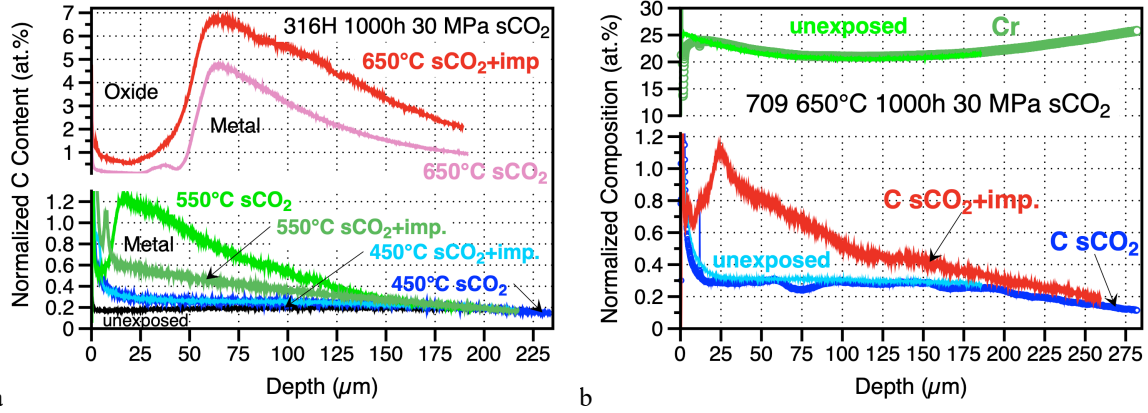


Figure 10: GDOES sputter depth profiles for 1000 h exposures in sCO₂ with and without impurities (a) 316H and (b) 709. In (b), both Cr and C profiles are shown.